The Shape of TiO$_2$-B Nanoparticles

Yuri G. Andreev,[†] Pooja M. Panchmatia,[‡] Zheng Liu,[†] Stephen C. Parker,[§] M. Saiful Islam,*[,§] and Peter G. Bruce*[,†]

[†]School of Chemistry, University of St Andrews, St Andrews KY16 9ST, U.K.

[‡]School of Applied Sciences, University of Huddersfield, Huddersfield HD1 3DH, U.K.

[§]Department of Chemistry, University of Bath, Bath BA2 7AY, U.K.

S *Supporting Information*

ABSTRACT: The shape of nanoparticles can be important in defining their properties. Establishing the exact shape of particles is a challenging task when the particles tend to agglomerate and their size is just a few nanometers. Here we report a structure refinement procedure for establishing the shape of nanoparticles using powder diffraction data. The method utilizes the fundamental formula of Debye coupled with a Monte Carlo-based optimization and has been successfully applied to TiO$_2$-B nanoparticles. Atomistic modeling and molecular dynamics simulations of ensembles of all the ions in the nanoparticle reveal surface hydroxylation as the underlying reason for the established shape and structural features.
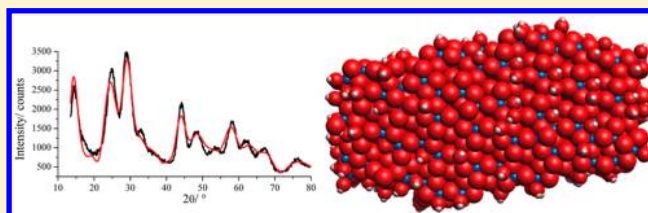
1. INTRODUCTION

Although the size of nanoparticles is usually regarded as their defining feature, their shape is also important.[1] Many of the properties of nanomaterials depend on their shape; for example, the properties of carbon nanotubes, fullerenes, and graphene sheets are all distinct, and the catalytic activity of oxide nanoparticles and electrochemical properties of intercalation electrodes for Li-ion batteries depend on their shape.[2−9]

Establishing the shape of nanoparticles may at first sight seem to be a trivial problem for transmission electron microscopy (TEM). However, nanoparticles often form in agglomerates, which makes determination of the primary particle shape a significant challenge. The peak shapes in powder X-ray and neutron diffraction depend on the size of the particles, microstrains, and stacking faults. Deconvolution through peak-shape analysis is possible but often problematical, especially when the sizes along different crystallographic directions are required in order to establish the shape of crystallites. Recently it has been demonstrated that pair distribution function (PDF) analysis can be used to distinguish between powders having the same elemental and phase composition but different particle shape by comparison of their PDFs.[10] Although successful in the case of nanoparticles with cubic (isotropic) symmetry, this method relies on differences in the PDF decay, which is also a function of the a priori unknown elemental composition of the relevant coordination spheres.

In this work, we used powder diffraction coupled with Debye refinement to establish the shape of nanoparticles and atomistic modeling to investigate the origin of the shape, exemplified specifically by application to TiO$_2$-B. In the course of Debye refinement, the entire powder X-ray diffraction pattern is fitted without recourse to symmetry or even crystallinity, to determine the particle shape. Atomistic modeling of the whole TiO$_2$-B nanoparticle using both energy minimization and molecular dynamics (MD) methods was essential in order to establish the origin of the shape. Atomistic simulation techniques have been used previously to predict the surface structures of materials composed of large (micrometer-sized) particles and hence their shape. For small nanoparticles, however, many of the atoms are no longer subjected exclusively to either bulk (symmetric) or surface (asymmetric) forces. As a result, it is necessary to simulate the total energy and structure of the ensemble, not just the surface, in determining the particle shape with a strong connection to experiment; this is what we have done here.

Surface hydroxylation is an important process to consider, as surface interactions with the solvent during synthesis can give rise to a certain degree of hydroxylation. It is known that OH groups produced upon dissociative water adsorption can strongly influence the properties of oxide particles, but there are limited combined experimental−modeling studies in this area. The effect of hydroxylation on the shape of TiO$_2$-B nanoparticles is not yet clear.

TiO$_2$-B nanoparticles were chosen because we have synthesized them with particularly small size, emphasizing the nano effect, and because they form as agglomerates. TiO$_2$-B has a structure distinct from those of the well-known rutile, anatase, and brookite polymorphs of titanium dioxide. It is by far the best host for lithium intercalation of any titanium dioxide, especially in nanoparticulate form.[4]

2. EXPERIMENTAL SECTION

TiO$_2$-B nanoparticles were synthesized using a hydrothermal method that has been described in detail elsewhere.[11] Individual particles are agglomerated in the TEM (JEOL JEM-2010) images (Figure 1), but their shape appears to be nonspherical, with a typical size between 2 and 5 nm.
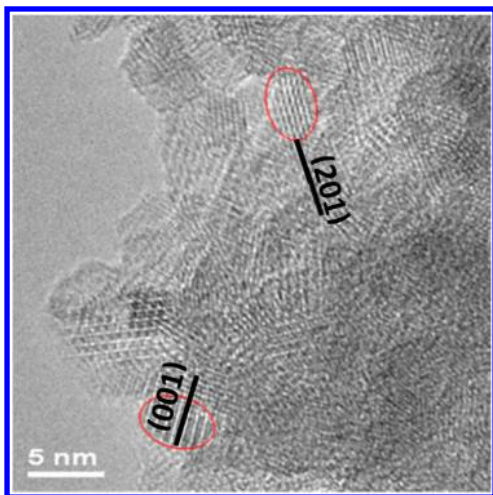

Figure 1. TEM image of TiO$_2$-B nanoparticles. Red lines outline individual particles. Black lines indicate the positions of (*hkl*) planes of the TiO$_2$-B structure in the particles, identified through distances between the observed lattice fringes.

Powder X-ray diffraction (Figure 2) confirmed previous studies showing that the synthesis procedure forms TiO$_2$-B. The data were
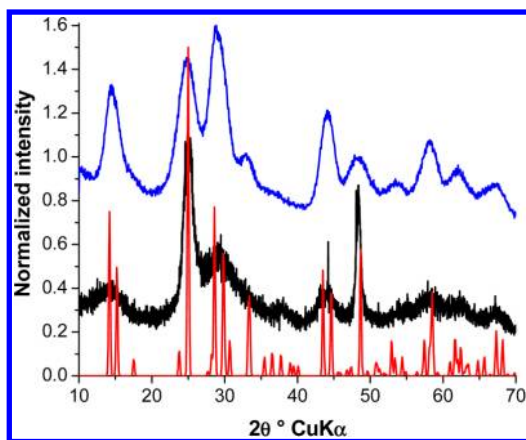

Figure 2. Powder X-ray diffraction patterns of TiO$_2$-B calculated from the ideal structural model (red) and observed for nanotubes (black)[12] and nanoparticles (blue).

collected in reflection mode in steps of 0.02° on a laboratory Philips diffractometer equipped with a graphite monochromator.

The absence of the commonly encountered anatase phase in hydrothermally prepared samples was verified by Raman spectroscopy (Figure S1 in the Supporting Information) using a Raman microscope equipped with a Nd:YAG laser (Toptica Photonics), a liquid-nitrogen-cooled CCD camera, and a Jobin Yvon iHr 550 spectrometer. The phase purity was further confirmed by the load curve during Li$^+$ intercalation,[11] which did not show signs of a flat plateau in the region between 1.75 and 1.90 V, typical of the anatase.[13]

Transmission Fourier Transform infrared (FTIR) spectroscopy (Nicolet 6700) indicated the presence of O–H stretches (Figure 3). No surfactant residue was found in the sample; the amount of residual
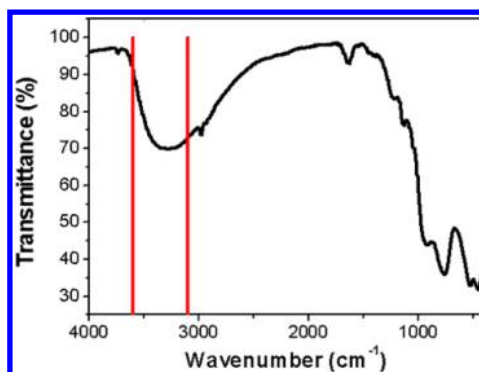

Figure 3. FTIR spectrum of TiO$_2$-B nanoparticles. Vertical lines indicate the range of characteristic absorptions of O–H stretches.

carbon was 0.3 wt %, which would correspond to a layer of carbon on the surface well below 1 Å in thickness.[11]

3. METHODS

By means of full-profile, Rietveld, or individual peak-fitting methods, values of the full width at half-maximum (FWHM) and integral breadth (IB) of individual peaks can be determined and analyzed to establish the crystallite size along various crystallographic directions.[14] Apart from the problem of relying on the validity of the empirical peak-shape function as well as the distribution functions for crystallite sizes and microstrains (both are the most likely sources of peak broadening), the two fitting methods require a well-defined background line in order to obtain trustworthy values of the FWHMs and IBs. The severe broadening of the diffraction peaks in the patterns of very small nanoparticles such as the TiO$_2$-B nanoparticles studied here (see Figure 2) precludes reliable identification of the background.

In the method of Warren and Averbach,[15] empirical functions, FWHMs, and IBs are not used, and the crystallite size is obtained through analysis of the Fourier coefficients of at least two Bragg peaks from the same crystallographic planes (e.g., 111 and 222). However, the nature of Fourier transformation imposes a strict requirement of reaching the background level on both sides of each reflection used in such analysis, making the latter suitable predominantly for high-symmetry crystal structures.

In recent years, PDF analysis[16,17] of powder diffraction data applied to crystalline compounds has been extended to the analysis of particle shape. It is based on a Fourier transform of the entire diffraction pattern, thus taking into account both diffuse and Bragg scattering, and does not rely on empirical functions or a priori assumptions of any kind. The technique is used primarily to probe local disorder. However, it has been shown that in some cases PDF analysis can provide information about the shape of nanoparticles, albeit indirectly, through comparison of density functions from nanoparticles and from a reference polycrystalline material.[10,18,19]

To investigate the structure, shape, and size of the TiO$_2$-B nanoparticles using powder diffraction, we have developed a refinement procedure based on first-principles diffraction theory that takes into account all types of scattering and operates in direct space without recourse to crystallography (symmetry) or empirical functions. To validate the refinement results and establish the underlying reasons for the observed shape of the nanoparticles, an advanced computational methodology for atomistic modeling was applied. The approach was developed to simulate explicitly the surfaces and shape of the TiO$_2$-B nanoparticles using a combination of energy minimization and MD techniques. An important aspect of the study was the simulation of hydroxylated surfaces in addition to pristine TiO$_2$-B.

3.1. Structure Refinement Using the Debye Equation. A powder diffraction pattern $I(\theta)$, collected in a constant-wavelength mode, can be calculated using the equation of Debye:

$$I(\theta) = \sum_n f_n^2(\theta) + 2 \sum_i \sum_j f_i(\theta) f_j(\theta) \frac{\sin(4\pi r_{ij} \sin\theta/\lambda)}{(4\pi r_{ij} \sin\theta/\lambda)}$$

where $f_n(\theta)$ is the atomic form factor of the nth atom in the scattering array, λ is the wavelength, and r_{ij} is the distance between atoms i and j.[20] The equation is exact in the kinematic (single scattering) approximation and describes Bragg and diffuse scattering as well as the small-angle scattering from a powder. The mathematical simplicity of the formula is more than counterbalanced by the computational expense of its use, since for any blind-drawn powder the distances r_{ij} between all atoms in the particle have to be calculated.

Structure refinement of the TiO_2-B nanoparticles was carried out by minimization of the χ^2 figure-of-merit function, calculated as a sum of weighted squared differences between the experimental and Debye-equation-calculated intensities. The r_{ij} values were computed from the coordinates of atoms in each trial nanoparticle. The latter was cut as an ellipsoid from the bulk TiO_2-B structure. The lattice parameters (a, b, c, β) of the bulk structure and the lengths of the ellipsoid axes (A, B, C) served as variables in the refinement. To account for deformations/strains, which are not uncommon in nano-objects and also lead to broadening of Bragg diffraction peaks, the atomic coordinates within the ellipsoid were modified as follows:

$$\begin{bmatrix} x_i^D \\ y_i^D \\ z_i^D \end{bmatrix} = \begin{bmatrix} 1+k & G_{xy} & G_{xz} \\ 0 & 1+l & G_{yz} \\ 0 & 0 & 1+m \end{bmatrix} \begin{bmatrix} x_i \\ y_i \\ z_i \end{bmatrix}$$

where k, l, and m represent coaxial strains and G_{xy}, G_{xz}, and G_{yz} are shear deformations, all serving as variable parameters. Finally, during the calculation of each r_{ij}, the coordinates of atoms i and j were randomly placed within the spheres centered at x_i^D, y_i^D, z_i^D and x_j^D, y_j^D, z_j^D, respectively, to mimic static or thermal isotropic mean-squared displacements. The radii of the spheres for Ti and O atoms, $(\langle U^2 \rangle^{1/2})_{Ti}$ and $(\langle U^2 \rangle^{1/2})_O$, were two additional variables in the refinement.

The discrete functional dependence $\chi^2(A, B, C)$ and the nonanalytical function $\chi^2[(\langle U^2 \rangle^{1/2})_{Ti}, (\langle U^2 \rangle^{1/2})_O]$ precluded the use of gradient least-squares as a minimization method. Global optimization by simulated annealing was employed to carry out the Debye refinement, using a protocol similar to that utilized in ab initio structure determination from powder diffraction data.[21] Such a Monte Carlo-based procedure was an additional burden on an already computationally expensive Debye algorithm.

The computational load in the refinement was significantly decreased by reducing the 2θ range on the lower-angle side, where Bragg scattering was not expected, and by taking into account only every fifth point in the diffraction pattern (increasing the step size in 2θ from 0.02° to 0.1°). In addition, the refinement code was written for a multiprocessor computer, with the task of calculating the value of the double sum in the Debye equation equally distributed among the processors and performed in parallel. The refinement was performed on a Dell PowerEdge T410 desktop workstation with 12 cores operating under LINUX.

3.2. Atomistic Modeling. The approach for modeling surface structures and nanoparticle shapes employs a powerful combination of efficient energy minimization methods and MD techniques, which can be performed independently;[22-25] these methods are based on effective interatomic potentials consisting of a sum of long-range Coulombic and short-range repulsive terms and are embodied in the simulation codes METADISE[26] and DLPOLY.[27] As argued previously,[23] the general transferability and accuracy of the derived potentials for oxide materials are assessed primarily by the reproduction of available experimental properties of the system. First, the set of potential model parameters[28,29] (Table S1 in the Supporting Information) accurately reproduces the structure of bulk TiO_2-B (space group $C2/m$), showing good comparison with neutron diffraction data (Table S2 in the Supporting Information). It is noted that these potentials have also reproduced the experimental structures and the relative order of stabilities of the anatase and rutile forms of

TiO_2,[28,29] which suggests that the potential model is reliable over a range of configurations, including nanoparticle structures.

For the initial simulations of crystalline TiO_2-B surfaces, planar two-dimensional periodic boundary conditions were applied to a block of crystal parallel to the plane of interest using well-established methodology.[22,23] Our potential-based techniques allow a large number of ions and surface planes to be treated, ensuring that the results are independent of model size. The energies of a wide range of surfaces of TiO_2-B were calculated, allowing full energy minimization. The thermodynamic equilibrium shape or morphology of the macroscopic crystal was obtained from the Wulff construction using these calculated surface energies. Such methods have been used successfully to examine surfaces and morphologies of a variety of oxide materials,[30-33] including other TiO_2 polymorphs.[34,35]

Our modeling approach then considered explicitly the structure and total energy of the ensemble of all the ions in the nanoparticle, not just the surface, in determining the particle shape. First, a charge-neutral nanocluster about 3 nm in size (~2900 ions) was generated by carving out a shape from the parent bulk structure based on the Wulff construction for pristine crystalline TiO_2-B. The nanocluster was energy-minimized in order to remove any unrealistic residual net forces. The subsequent MD simulations were used to overcome any local energy minima and were performed in the NVT ensemble (for 1 ns, time step of 0.2 fs, temperature of 300 K). The nanoparticle was treated explicitly with no periodic boundary conditions imposed and full calculation of all the interionic interactions defined by the potential model. To explore the energy landscape, scans of different starting configurations were performed, varying the position of the particle origin. Previous MD simulation studies include work on rutile and anatase nanoparticles.[36,37] It is worth noting that potentials-based MD simulations can now be run regularly for time scales on the order of nanoseconds, which is at least 2 orders of magnitude longer than ab initio MD calculations of much smaller cell sizes. Indeed, the advantage of interatomic potential methods is that they are computationally inexpensive and thus allow nanoparticles of large ensembles of atoms (>1000) to be handled efficiently.

Computational investigations of water on bulk crystalline surfaces of TiO_2 have been reported.[38-40] However, the effect of hydroxylation on the shape of titania nanoparticles is yet to be established. Here the entire particle shape was recalculated with full, 75%, 50%, and 25% monolayer coverages of the surface by hydroxyl groups (on undercoordinated surface Ti sites) and protons (at surface O sites). MD simulation scans of different starting configurations for 1 ns at 300 K were performed, which allowed the construction of hydroxylated nanoparticles. It is noted that these atomistic simulations of the shape of the nanoparticle are a necessary precursor to explicit ab initio calculations on lithium intercalation into the nanoparticle, which are part of ongoing work.

4. RESULTS AND DISCUSSION

Powder diffraction data from TiO_2-B nanoparticles reveal anisotropic peak broadening. Although less pronounced than in the case of TiO_2-B nanotubes (see Figure 2), where the 010 reflection at ~48.5° is markedly narrower than the rest because the crystallographic b axis is parallel to the tube axis,[11] differences in the peak widths are also apparent for the nanoparticles. Thus, the width of the peak at ~28.9°, which comprises four reflections (002, 40$\bar{1}$, 111, and 400), is smaller than that of the peak at ~24.8°, which is a single 110 reflection. Similarly, the width of the 010 peak from the nanoparticles is greater than that of the peak at ~44.2° consisting of 003 and 60$\bar{1}$ reflections.

Further evidence of the anisotropic broadening was found through comparison of peak-amplitude values in the above examples. The observed maximum-count ratio for the peaks at 24.8° and 28.9° could be matched by the calculated bulk intensities only if all four reflections have exactly the same 2θ
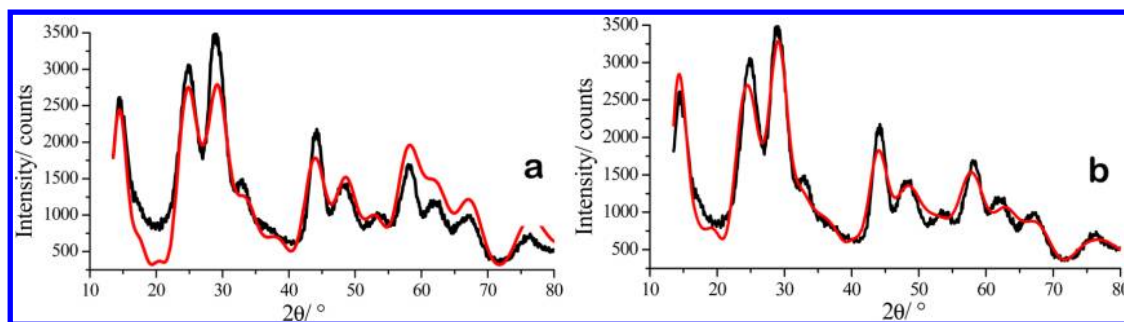
Figure 4. Debye refinement of the structure of a TiO$_2$-B nanoparticle. (a) Fit using a spherical particle with the ideal TiO$_2$-B structure as the starting model. (b) Final fit with the refined structure. Black lines represent experimental data. Red lines show values calculated using the respective models.

position, while in fact they are spread over the interval of 2°. All of this points to an anisotropic shape for the nanoparticles.

Spherical particles with a diameter of 3 nm having the ideal crystal structure of TiO$_2$-B served as a starting model for Debye refinement. Such a model provided a poor fit to the experimental data (Figure 4a). In the course of the refinement, ~94 000 powder patterns were calculated and compared to the experimental pattern, and ~11 000 were accepted by the Metropolis sampling algorithm within the simulated annealing minimization procedure. The minimization terminated properly when the system "froze" (i.e., no uphill or downhill steps accepted at the given "temperature"). The final fit to the experimental data is shown in Figure 4b, and the starting and final values of the variable parameters are listed in Table 1.

Table 1. Structural Parameters of a TiO$_2$-B Nanoparticle

parameter	starting model	refined model
lattice parameter a (Å)	12.18	12.324(2)
lattice parameter b (Å)	3.74	3.744(2)
lattice parameter c (Å)	6.52	6.458(2)
lattice parameter β (deg)	107.03	108(1)
ellipsoid axis A (nm)	3.0	2.4(2)
ellipsoid axis B (nm)	3.0	2.5(2)
ellipsoid axis C (nm)	3.0	3.9(2)
coaxial strain along a, k	0.000	−0.027(3)
coaxial strain along b, l	0.000	0.002(3)
coaxial strain along c, m	0.000	−0.005(3)
shear deformation G_{xy}	0.000	>-0.001
shear deformation G_{xz}	0.000	<0.001
shear deformation G_{yz}	0.000	0.001(6)
$(\langle U^2 \rangle^{1/2})_{Ti}$ (Å)	0.00	0.63(2)
$(\langle U^2 \rangle^{1/2})_{O}$ (Å)	0.00	0.55(2)
χ^2	64.9	12.0

The refinement did not reveal any significant variations in the lattice parameters of the nanoparticles, with the maximum deviation being 1.2% in the value of a. No significant strains/deformations were detected in the TiO$_2$-B particles, which is unusual for particles of such high surface-to-volume ratio.[41,42] High surface energy is expected to cause strain. The greater

than 5-fold improvement in the fit was gained from the refined anisotropic shape of the particles (different dimensions in different crystallographic directions) and, to a lesser extent, from higher amplitudes of the mean-square displacements of atoms than are typical in bulk materials. The particle shape is adequately described by an ellipsoid, the longer axis of which coincides with the c crystallographic direction and is 1.6 times longer than the other two axes, which are approximately the same length. The remaining mismatches in the final fit were most likely caused by the distribution of the shapes and sizes of the particles in the powder sample from which the experimental data were collected.

Turning to the modeling investigation, potentials-based techniques (described in Methods) were employed to calculate the surface structures and energies for numerous crystal orientations of pristine TiO$_2$-B. It is noted that because of the cell sizes, most previous density functional theory (DFT) studies on oxide surfaces modeled only a few low-index surface planes.

The calculated surface energies for pristine TiO$_2$-B are listed in Table 2. The majority of the surfaces undergo considerable decreases in surface energy from the unrelaxed structures, typically 50–80%, resulting in increased stability of the terminating layers. This shows the importance of relaxation at the particle surface and indicates that the relative surface energies cannot be reliably predicted by assuming the oxide surface to be a rigid, unrelaxed termination of the crystal lattice.

The crystal morphology predicted from the surface energies is shown in Figure 5. For nanosized particles, where rearrangement of the crystal at each stage of the growth is possible, a morphology close to the equilibrium form might be expected. The lowest surface energies for pristine TiO$_2$-B were found for the (001), (110) and (100) surfaces, which are prominent in the particle morphology. Using this Wulff construction, a charge-neutral nanocluster 3 nm in size was generated and optimized for a pristine TiO$_2$-B nanoparticle. As noted above, our energy minimization and MD approach considers explicitly the structure and total energy of the ensemble of all the ions in the nanoparticle, not just the surface, in determining the particle shape. The resulting nanoparticle shape (shown in Figure 6) is in effect isotropic, which may not

Table 2. Relaxed Surface Energies (J m^{-2}) of Pristine and Hydroxylated TiO$_2$-B Crystalline Surfaces

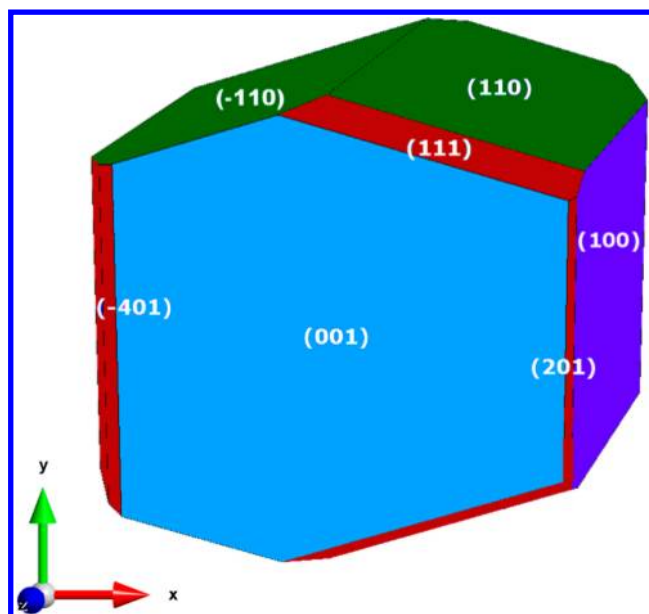|	(001)	(110)	(100)	(010)	(111)	(201)	(−201)	(−401)	(−601)
pristine	1.05	1.16	1.21	1.27	1.39	1.39	1.67	1.53	1.55
hydroxylated[a]	1.30	0.79	0.74	0.89	1.59	1.68	1.14	0.57	0.94

[a]75% coverage.

Figure 5. Equilibrium shape of a pristine crystalline particle of TiO_2-B using the calculated surface energies.
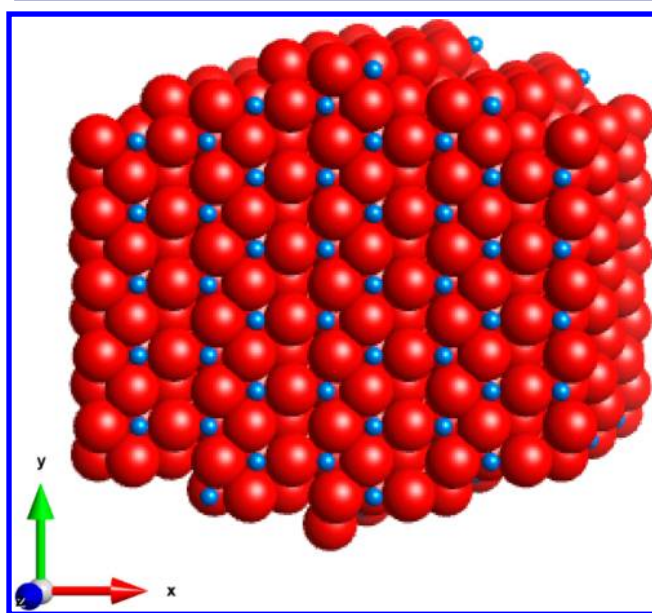

Figure 6. Simulated shape of a pristine nanoparticle about 3 nm in size (blue and red spheres denote Ti and O, respectively).

Figure 7. Debye equation powder diffraction patterns of TiO_2-B nanoparticles: experimental (black crosses) and calculated using pristine (blue) and hydroxylated (red) nanoparticle structures derived from atomistic modeling.

Such hydroxylation of the surfaces significantly changes the surface energies and hence the relative energy balance between the various facets (see Table 2). Consequently, the change in the total energies leads to a different and more elongated equilibrium shape of the crystalline particle (Figure 8).

Figure 8. Equilibrium shape of a hydroxylated crystalline particle of TiO_2-B based on calculated surface energies.

Moreover, the resulting shape of the hydroxylated nanoparticle is close to that of an ellipsoid; the longer axis of the simulated particle parallel to the c crystallographic direction is in good accord with that obtained in the course of the Debye refinement, apart from slightly higher aspect ratios (C/A = 1.79, C/B = 1.72), although the difference $C/A − C/B$ is comparable.

The powder pattern calculated for the simulated hydroxylated nanoparticle of ellipsoidal shape (Figure 9) matches the experimental profile significantly better than the pattern of isotropic form does, particularly in the angular range 12−56° (see Figure 7); there is a reduction of fit in the range 56−65°, most likely caused by the uncertainty in the extent of the surface coverage or, less likely, by the small number of other groups attached to the surface. Nevertheless, the results show good quantitative accord and indicate that an underlying reason for the formation of an ellipsoidal shape is the hydroxylation of the surface in the course of hydrothermal synthesis.

It is apparent that the precise surface planes are not easily assigned from experiment, particularly given the small sizes of the particles. Inspection of the simulated nanoparticle indicates

be surprising since the maximum difference in surface energies amounts to ∼30%.

Using this isotropic nanoparticle structure to calculate the powder diffraction pattern resulted in the simulation shown in Figure 7. The match to the experimental pattern is poor. Since OH stretches were detected in the FTIR spectrum from the TiO_2-B nanoparticles (see Figure 3), the entire particle (including surface energies) was recalculated with, as noted above, full, 75%, 50%, and 25% monolayer coverages of the surface by hydroxyl groups (Ti sites) and protons (O sites). MD simulation scans of different starting configurations allowed the construction of hydroxylated nanoparticles about 3 nm in size. The nanoparticle structure with 75% coverage was found to be the most stable and showed the closest accord with the observed shape.
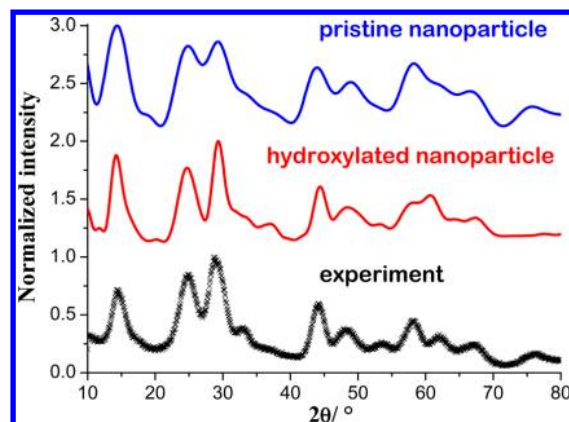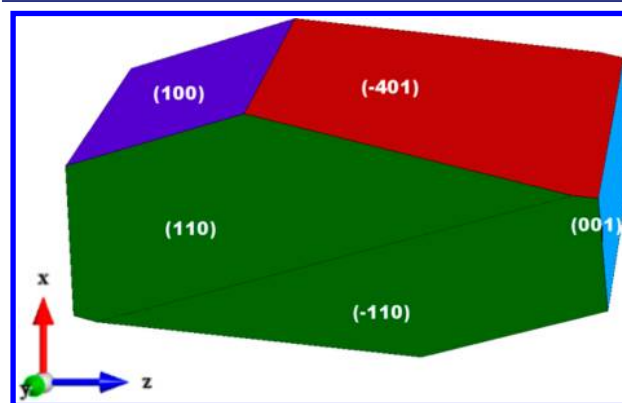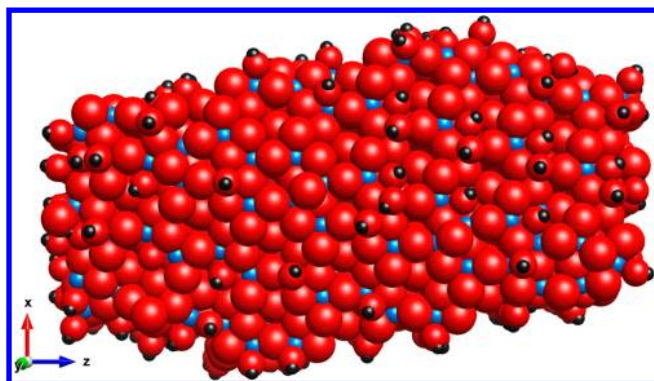
Figure 9. Simulated ellipsoid shape of a hydroxylated nanoparticle (blue, red, and black spheres denote Ti, O, and H, respectively).

the expression of microfacets corresponding to the (110), (001), (100), and (401) surfaces of crystalline TiO$_2$-B. These surfaces are expected to play a significant role in the electrochemical and surface-exchange properties of the material. Our previous DFT study of lithium insertion in bulk TiO$_2$-B[43] found that Li-ion transport is favorable along the [010] b axis channels and the c direction, complementing other ab initio studies on Li/TiO$_2$-B.[44−47] The (110) and (001) surfaces are of particular interest because they allow access to these Li$^+$ diffusion pathways, which may help expedite the reversible Li$^+$ intercalation process.

5. CONCLUDING REMARKS

Structure refinement based on the Debye equation is a powerful tool for establishing the shape and structure of nanoparticles. When combined with atomistic and MD modeling, it provides insight into the origin of the observed shapes and structural features on the atomic scale.

The Debye studies revealed that the shape of the TiO$_2$-B nanoparticles is close to that of an ellipsoid. Modeling of ensembles of all the ions in the nanoparticle showed that the underlying reason for the formation of such a shape is the hydroxylation of the surface in the course of hydrothermal synthesis. The simulated ellipsoid shape of the hydroxylated nanoparticle is in good accord with the observed shape from the Debye refinement. The powder pattern generated from this simulated atomic-level structure also matches the experimental profile considerably better than that for a nanoparticle without a hydrated surface. Indeed, a key challenge in the modeling of nanomaterials is making direct links with experiment.

The OH groups greatly modify the surface and total energies of the nanoparticle relative to the pristine form by helping to minimize surface strains and distortions of certain facets of the nanoparticle, which is not uncommon when the surface-to-volume ratio is high. This also explains the negligible strain values established in the course of the Debye refinement. Significant strains are often observed in nanoparticles arising from the forces akin to surface tension, something the hydration relieves. The exposure of the (110) and (001) facets is significant for electrode function since this would allow access to the most facile pathways for lithium-ion diffusion and hence would be important for the reversible insertion/deinsertion of lithium ions.

■ AUTHOR INFORMATION

Corresponding Authors
p.g.bruce@st-andrews.ac.uk
m.s.islam@bath.ac.uk

Notes
The authors declare no competing financial interest.

■ REFERENCES

(1) Nanomaterial Properties: Size and Shape Dependencies (special issue): Guisbiers, G.; Mejía-Rosales, S.; Deepak, F. L. *J. Nanomater.* **2012**, *2012*, No. 180976, and related articles.
(2) Dinadayalane, T. C.; Leszczynski, J. *Struct. Chem.* **2010**, *21*, 1155−1169.
(3) Ariga, K.; Ji, Q.; McShane, M. J.; Lvov, Y. M.; Vinu, A.; Hill, J. P. *Chem. Mater.* **2012**, *24*, 728−737.
(4) Armstrong, A. R.; Armstrong, G.; Canales, J.; Bruce, P. G. *Angew. Chem., Int. Ed.* **2004**, *43*, 2286−2288.
(5) Wagemaker, M.; Mulder, F. M. *Acc. Chem. Res.* **2013**, *46*, 1206−1215.
(6) Zhou, Z. Y.; Tian, N.; Li, J. T.; Broadwell, I.; Sun, S. G. *Chem. Soc. Rev.* **2011**, *40*, 4167−4185.
(7) Pumera, M. *Chem. Soc. Rev.* **2010**, *39*, 4146−4157.
(8) Arico, A. S.; Bruce, P. G.; Scrosati, B.; Tarascon, J. M.; van Schalkwijk, W. *Nat. Mater.* **2005**, *4*, 366−377.
(9) Maier, J. *Nat. Mater.* **2005**, *4*, 805−815.
(10) Petkov, V.; Cozzoli, P. D.; Buonsanti, R.; Cingolani, R.; Ren, Y. *J. Am. Chem. Soc.* **2009**, *131*, 14264−14266.
(11) Ren, Y.; Liu, Z.; Pourpoint, F.; Armstrong, A. R.; Grey, C. P.; Bruce, P. G. *Angew. Chem., Int. Ed.* **2012**, *51*, 2164−2167.
(12) Andreev, Y. G.; Bruce, P. G. *J. Am. Chem. Soc.* **2008**, *130*, 9931−9934.
(13) Gentili, V.; Brutti, S.; Hardwick, L. J.; Armstrong, A. R.; Panero, S.; Bruce, P. G. *Chem. Mater.* **2012**, *24*, 4468−4476.
(14) *The Rietveld Method*; Young, R. A., Ed.; Oxford University Press: New York, 1996.
(15) Warren, B. E.; Averbach, B. L. *J. Appl. Phys.* **1952**, *23*, 497.
(16) Kitaigorodsky, A. I. *X-ray Structural Analysis of Microcrystalline and Amorphous Substances*; Gostekhizdat: Moscow, 1952.
(17) Guinier, A. *X-ray Diffraction in Crystals, Imperfect Crystals and Amorphous Bodies*; W. H. Freeman: San Francisco, 1963.
(18) Wang, H.-W.; Wesolowski, D. J.; Proffen, T. E.; Vlcek, L.; Wang, W.; Allard, L. F.; Kolesnikov, A. I.; Feygenson, M.; Anovitz, L. M.; Paul, R. L. *J. Am. Chem. Soc.* **2013**, *135*, 6885−6895.
(19) Jensen, K. M. O.; Christensen, M.; Juhas, P.; Tyrsted, C.; Bojesen, E. D.; Lock, N.; Billinge, S. J. L.; Iversen, B. B. *J. Am. Chem. Soc.* **2012**, *134*, 6785−6792.
(20) Debye, P. *Ann. Phys.* **1915**, *351*, 809−823.
(21) Andreev, Y. G.; Lightfoot, P.; Bruce, P. G. *J. Appl. Crystallogr.* **1997**, *30*, 294−305.
(22) *Computer Modeling in Inorganic Crystallography*; Catlow, C. R. A., Ed.; Academic Press: San Diego, CA, 1997.

(23) *Computational Methods for Energy Materials*; Walsh, A., Sokol, A. A., Catlow, C. R. A., Eds.; John Wiley & Sons: Chichester, U.K., 2013.

(24) Spagnoli, D.; Gale, J. G. *Nanoscale* **2012**, *4*, 1051−1067.

(25) Islam, M. S.; Fisher, C. A. J. *Chem. Soc. Rev.* **2014**, *43*, 185−204.

(26) Watson, G.; Kelsey, E. T.; deLeeuw, N. H.; Harris, D. J.; Parker, S. C. *J. Chem. Soc., Faraday Trans.* **1996**, *92*, 433−438.

(27) Smith, W.; Forester, T. R. *J. Mol. Graphics* **1996**, *14*, 136−141.

(28) Kerisit, S.; Rosso, K. M.; Yang, Z.; Liu, J. *J. Phys. Chem. C* **2010**, *114*, 19096−19107.

(29) Matsui, M.; Akaogi, M. *Mol. Simul.* **1991**, *6*, 239−244.

(30) Fisher, C. A. J.; Islam, M. S. *J. Mater. Chem.* **2008**, *18*, 1209−1215.

(31) Sayle, T. X. T.; Parker, S. C.; Sayle, D. C. *Chem. Commun.* **2004**, 2438−2439. Titiloye, J. O.; Parker, S. C.; Osguthorpe, D. J.; Mann, S. *J. Chem. Soc., Chem. Commun.* **1991**, 1494−1496.

(32) Sayle, D. C.; Feng, X.; Ding, Y.; Wang, Z. L.; Sayle, T. X. T. *J. Am. Chem. Soc.* **2007**, *129*, 7924−7935.

(33) Bromley, S. T.; Moreira, I. P. R.; Neyman, K. M.; Illas, F. *Chem. Soc. Rev.* **2009**, *38*, 2657−2670.

(34) Howard, A.; Mitchell, S. E. J.; Morris, D.; Egdell, R. G.; Parker, S. C. *Surf. Sci.* **2000**, *448*, 131−141.

(35) Oliver, P. M.; Watson, G. W.; Kelsey, E. T.; Parker, S. C. *J. Mater. Chem.* **1997**, *7*, 563−568. Olson, C. L.; Nelson, J.; Islam, M. S. *J. Phys. Chem. B* **2006**, *110*, 9995−10001.

(36) Zhang, H. Z.; Banfield, J. F. *J. Phys. Chem. C* **2007**, *111*, 6621−6629.

(37) Naicker, P. K.; Cummings, P. T.; Zhang, H. Z.; Banfield, J. F. *J. Phys. Chem. B* **2005**, *109*, 15243−15249.

(38) Hoffmann, M. R.; Martin, S. T.; Choi, W.; Bahnemann, D. W. *Chem. Rev.* **1995**, *95*, 69−96.

(39) Sun, C.; Liu, L. M.; Selloni, A.; Lu, G. Q.; Smith, S. C. *J. Mater. Chem.* **2010**, *20*, 10319−10334.

(40) Vittadini, A.; Casarin, M.; Selloni, A. *J. Mater. Chem.* **2010**, *20*, 5871−5877.

(41) Andreev, Y. G.; Burkhanov, A. V.; Ermolaev, A. G.; Zelenyuk, F. M.; Lapovok, V. N.; Petrunin, V. F.; Sukhovich, E. P.; Trusov, L. I. *Phys. Chem. Mech. Surf.* **1990**, *5*, 2560−2571.

(42) *Nanoalloys: Synthesis, Structure and Properties*; Alloyeau, D., Mottet, C., Ricolleau, C., Eds; Springer: London, 2012.

(43) Arrouvel, C.; Parker, S. C.; Islam, M. S. *Chem. Mater.* **2009**, *21*, 4778−4783.

(44) Panduwinta, D.; Gale, J. D. *J. Mater. Chem.* **2009**, *19*, 3931−3940.

(45) Morgan, B. J.; Watson, G. W. *Phys. Rev. B* **2010**, *82*, No. 144119.

(46) Dalton, A. S.; Belak, A. A.; Van der Ven, A. *Chem. Mater.* **2012**, *24*, 1568−1574.

(47) Dylla, A. G.; Xiao, P.; Henkelman, G.; Stevenson, K. J. *J. Phys. Chem. Lett.* **2012**, *3*, 2015−2019.